Nonlinear dynamics in an optical system with controlled two-dimensional feedback: Black-eye patterns and related phenomena

M. A. Vorontsov[1] and B. A. Samson[1,2]

[1]*Army Research Laboratory, Adelphi, Maryland 20783*
[2]*Institute of Physics, Belarus Academy of Sciences, Minsk, Belarus*

We present experimental and theoretical results of spontaneous optical pattern formation in a nonlinear optical system. The nonlinear optical system we considered had a controllable phase-only spatial Fourier filter placed in the system's diffractive feedback loop. A change in feedback field spatial spectral component phase resulted in a transition between dynamic regimes, as observed in both experiments and numerics. Patterns originating from interactions between spatial modes belonging to different instability bands (black-eye patterns, decagons, etc.) were observed, as well as localized states and shock traveling waves. [S1050-2947(98)02304-X]

I. INTRODUCTION

Pattern formation is one of the fastest growing fields in modern optics. Both the number of nonlinear optical systems capable of generating transverse patterns [1–10] and the number of patterns that can coexist and compete in the same system [11–14] continue to increase. From a beginning with simple patterns originating from nonlinear interactions between only a few modes [1,15], pattern formation studies now involve analysis of sophisticated spatio-temporal regimes that include interactions of dozens of modes [14,16], formation of localized states [17–19] and transverse traveling waves [20], the excitation of spatio-temporal oscillations [21], and chaotic regimes [22]. A promising new trend in this field is spatio-temporal dynamics control [23–25].

We consider here a nonlinear optical system based on a liquid-crystal light-valve (LCLV) phase modulator with diffractive feedback. An additional phase-only spatial Fourier filter (computer-controlled multielement spatial phase modulator) is placed into the feedback loop to control phase shifts of the feedback field spatial spectral components.

In conventional nonlinear systems with diffractive feedback such as the Kerr-slice feedback mirror system [26] and LCLV or liquid crystal (LC) slice [27,5] based systems, pattern formation dynamics depend on feedback field diffraction, which leads to spatial frequency dependent phase shifts ϕ^d between feedback field spectral components. For free-space propagation these phase shifts are proportional to the square of the transverse wave vector $\boldsymbol{q}$: $\phi^d(\boldsymbol{q}) = q^2 L/(2k)$, where $q = |\boldsymbol{q}|$ is the transverse wave number, L is the length of diffraction, and $k = 2\pi/\lambda$ [15]. In the nonlinear optical system considered here we introduce additional phase shifts $\phi^c(\boldsymbol{q})$ to provide control of the feedback field spectral component phase. This results in the generation of symmetric patterns, waves, localized states, and spatio-temporal instabilities.

Experiments were performed using simple phase Fourier filters to control the phase within a small spectral domain region. In both theory and numerics we assume control of a single spectral component $\phi^c(\boldsymbol{q}_0) = \nu$, where ν is the phase shift amplitude. Depending on the wave vector $\boldsymbol{q}_0$ location and the phase shift amplitude ν, we observed the formation of spontaneous patterns including hexagons, rolls, black-eye patterns, and decagons, as well as localized states and traveling waves. Our theoretical analysis and numerical simulations for the black-eye patterns are in good agreement with the experimental data.

II. NONLINEAR SYSTEM WITH CONTROLLED FEEDBACK: EXPERIMENTAL RESULTS

A. Experimental setup

The experimental setup schematically shown in Fig. 1 is the LCLV diffractive feedback system first introduced in [27], with an additional Fourier spatial filter located in the
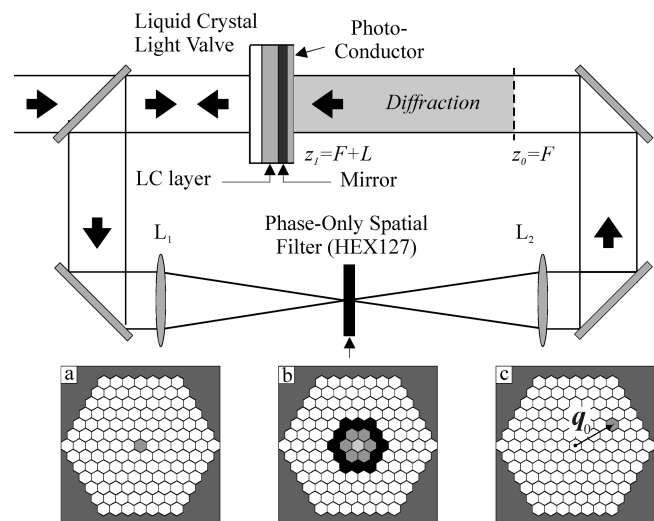

FIG. 1. Experimental setup and (a)–(c) LC phase modulator electrode maps: (a) Zernike-type spatial filter, (b) spatial filter composed of concentric rings, (c) spatial filter controlling off-axis spectral component. Gray levels indicate different voltage amplitudes applied to the corresponding LC elements. White hexagons correspond to zero voltage (no phase shift). Vector $\boldsymbol{q}_0$ shows the location of an off-axis element.

feedback loop. The Fourier spatial filter consisted of lenses L_1 and L_2 with focal length $F = 100$ cm, and a Hex-127 LC spatial phase modulator from Meadowlark Optics placed in the joint focal plane. This phase modulator has 127 individually addressed hexagonal LC cells, as shown in Figs. 1(a)–1(c). The size of each LC cell is 1.0 mm. Phase modulation depth ranged from 0 to 2π ($\lambda = 0.514$ mm) and was controlled by a computer. The LCLV was located in the front focal plane of L_1. The length of the diffractive path L (from $z_0 = F$ to $z_1 = F + L$ in Fig. 1 was varied by changing the distance z between lens L_2 and the LCLV's photoconductive layer. The case $z_1 < F$ corresponds to negative feedback diffractive lengths ($L < 0$), as described in [28].

In our experiments we used spatial filters with phase-only transfer functions such as $T(\boldsymbol{q}) = \exp[iQ(\boldsymbol{q})]$, where $\boldsymbol{q} = \boldsymbol{r}_F / (\lambda F)$ and $\boldsymbol{r}_F$ is a transverse vector in the spatial filter Fourier plane. Function $Q(\boldsymbol{q}) \equiv Q(\boldsymbol{r}_F)$ can be represented in the form $Q(\boldsymbol{r}_F) = \Sigma_{j=1}^{N} \nu_j S_j(\boldsymbol{r}_F)$, where ν_j are controlling voltages applied to the LC elements and $S_j(\boldsymbol{r}_F)$ are stepwise response functions corresponding to each LC element ($N = 127$). The following phase filters were implemented.

(i) A Zernike-type spatial filter [Fig. 1(a)]. The controlling voltage was applied only to the central ($j = 1$) LC element ($\nu_1 = \nu^{(0)}$ and $\nu_j = 0$ for $j > 1$). This filter provided phase control only for low-frequency spectral components. Since the diffraction-limited size of the input beam spatial spectrum was comparable to the LC element size, this Fourier filter can be considered as a Zernike-type filter that controls the phase of the zero spectral component [29].

(ii) As shown in Fig. 1(b), a filter providing phase control to the central element and the elements in the two concentric rings surrounding the central element ($\nu_1 = \nu^{(0)}, \nu_j = \nu^{(1)}$ for $j = 2, \ldots, 7$ and $\nu_j = \nu^{(2)}$ for $j = 8, \ldots, 19$).

(iii) Shown in Fig. 1(c), a filter controlling the phase of a single off-axis lth element $\nu_l = \nu^{(0)}$, $l \neq 1$, and $\nu_{j \neq l} = 0$.

The experimental setup shown in Fig. 1 was also used to analyze patterns originating from nonlinear interactions between an inserted image's spatial components and its self-induced modes (stimulated patterns [30]). Masks (inserted images) having an intensity transmission coefficient $M(\boldsymbol{r})$ were placed at the LCLV photoconductive layer plane $z_1 = F + L$.

B. Zero spectral component control

By controlling the phase shift of the feedback field zero spectral component, we were able to generate various patterns. Some of the patterns we observed are shown in Figs. 2. A negative diffractive length with various voltages applied to the phase modulator central element was used for Figs. 2(a)–2(d). Within the phase shift range $\nu^{(0)} \approx 0$ to $\nu^{(0)} \approx 0.35\pi$ we found only the hexagon-type patterns shown in Fig. 2(a). For $0.35\pi < \nu^{(0)} < 0.4\pi$ these hexagon-type patterns were transformed into a disordered array of patterns resembling black eyes, seen in Fig. 2(b). When the input field intensity was increased, instead of black eyes the patterns shown in Fig. 2(c) were observed. Further increases in the phase shift value $\nu^{(0)}$ resulted in a decrease in the number of black eyes. When $0.5\pi < \nu^{(0)} < 0.75\pi$, patterns consisting of only a few localized black eyes visible on a high-frequency hexagon
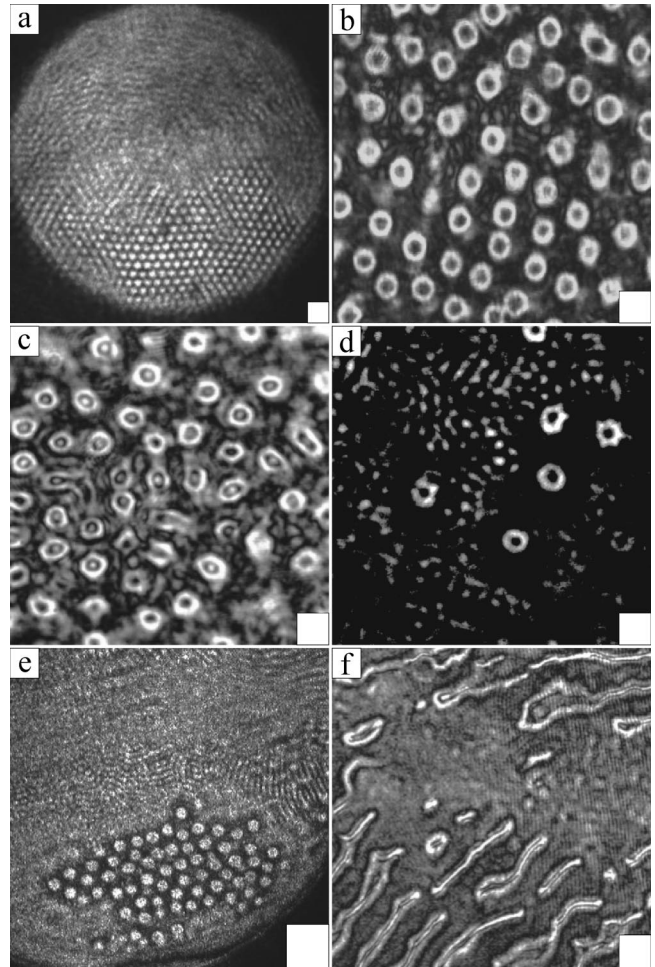

FIG. 2. Experimentally observed transverse intensity distributions of the output beam (plane $z = z_1$) corresponding to $L = -20$ cm [(a)–(d)] and $L = 20$ cm [(e) and (f)] for different $\nu^{(0)}$: (a) hexagonal array ($\nu^{(0)} = 0$), (b) disordered array of black eyes ($\nu^{(0)} = 0.4\pi$), (c) black eyes with pupils ($\nu^{(0)} = 0.4\pi$), (d) localized black eyes ($\nu^{(0)} = 0.65\pi$), (e) island of localized bright spots ($\nu^{(0)} = 0.75\pi$), (f) optical squirms ($\nu^{(0)} = 1.1\pi$). The white square on the bottom right represents 1 mm for (a) and (e), and 0.5 mm for the rest.

background, as seen in Fig. 2(d), appeared. We did not observe regular patterns in the range $0.75\pi < \nu^{(0)} < 2.0\pi$.

When the diffractive length was positive and as $\nu^{(0)}$ was increased, we found hexagonal type patterns ($0 < \nu^{(0)} < 0.5\pi$), islands of hexagons as in Fig. 2(e) ($0.6\pi < \nu^{(0)} < 0.75\pi$), localized bright spots on a hexagon-type background ($0.8\pi < \nu^{(0)} < 0.9\pi$), and the complicated pattern shown in Fig. 2(f).

Far field patterns (spatial spectra of the field at z_1) that occur far beyond the threshold conditions for various $\nu^{(0)}$ are presented in Fig. 3. In all observed cases the spatial spectra consisted of concentric rings (instability cones [11] or instability balloons [31]) that determine the location of the most unstable spatial mode wave vectors. Near the onset of an instability threshold the spatial spectrum had six dominating well-pronounced components located on the instability ring. By controlling the phase of the zero-order spectral component, we were able to change the instability ring radii, illustrated in Figs. 3(a)–3(c). The spatial spectrum in Fig. 3(d)
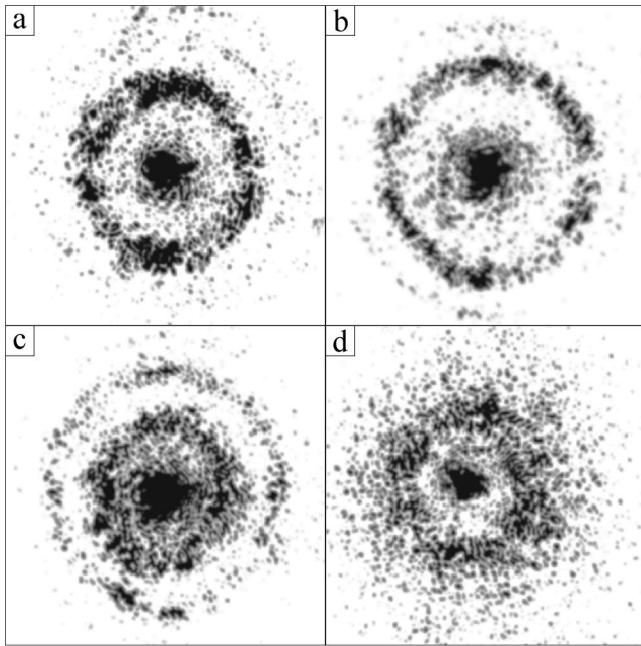
FIG. 3. Output field spatial spectra for different phase shift amplitudes $\nu^{(0)}$: (a) $\nu^{(0)}=0$, (b) $\nu^{(0)}=\pi/2$, (c) $\nu^{(0)}=\pi$, (d) $\nu^{(0)}=0.4\pi$. $L=20$ cm for (a)–(c) and $L=-20$ cm for (d). The central black spot diameter is approximately equivalent to a single LC cell size ($\sim$1 mm).

corresponds to the black-eye pattern shown in Fig. 2(b). In comparison with the spatial spectra for hexagonal-type patterns, the spectrum for the black-eye pattern has less distinct instability rings and a wider instability spectral band.

Optical noise in the LCLV caused by inhomogeneity in sensitivity of the LCLV's photosensitive layer, as well as inhomogeneities in the input beam phase and intensity distributions, did not allow us to obtain regular patterns for the entire laser beam aperture. In order to stabilize the output patterns, amplitude masks $M(\mathbf{r})$ with different symmetries were placed into the feedback loop, leading to the formation of stimulated patterns. A hexagonal gray scale mask of the type $M(\mathbf{r})\propto\Sigma_{j=1}^{3}[\cos(\mathbf{q}_j\cdot\mathbf{r})+1]$, where vectors $\mathbf{q}_j$ ($j=1,2,3$) form an equilateral triangle, was used to stabilize the irregular black-eye array in Fig. 2(b). The mask's spatial frequency of $q_A=|\mathbf{q}_j|$ was approximately equal to the spatial frequency $q_d=\sqrt{\pi k/L}$ for the hexagonal array in the system without Fourier filter ($\nu^{(0)}=0$). In the presence of the mask, the irregular black-eye pattern in Fig. 2(b) was transformed into the black-eye hexagonal array shown in Fig. 4(a).

To analyze the effect of different spatial spectral components on black-eye pattern formation, we placed an amplitude low-pass filter with variable cutoff frequency $q_{\mathrm{cut}}=r_F^{(0)}/(\lambda F)$ into the system's Fourier plane. When the amplitude filter radius $r_F^{(0)}$ was decreased, we observed a transition from the black-eye hexagonal array shown in Fig. 4(a) to the conventional hexagonal pattern in Fig. 4(b).

Black eyes arranged in a hexagon lattice were first observed in a chemical reaction-diffusion experiment: a chlorite-iodide-malonic acid reaction in a thin gel layer reactor [32]. These chemically produced black-eye patterns appeared to have spectral components with different wave numbers, similar to the pattern in Figs. 4(a) and 4(c). This suggests a common origin of the black-eye pattern in both experiments.
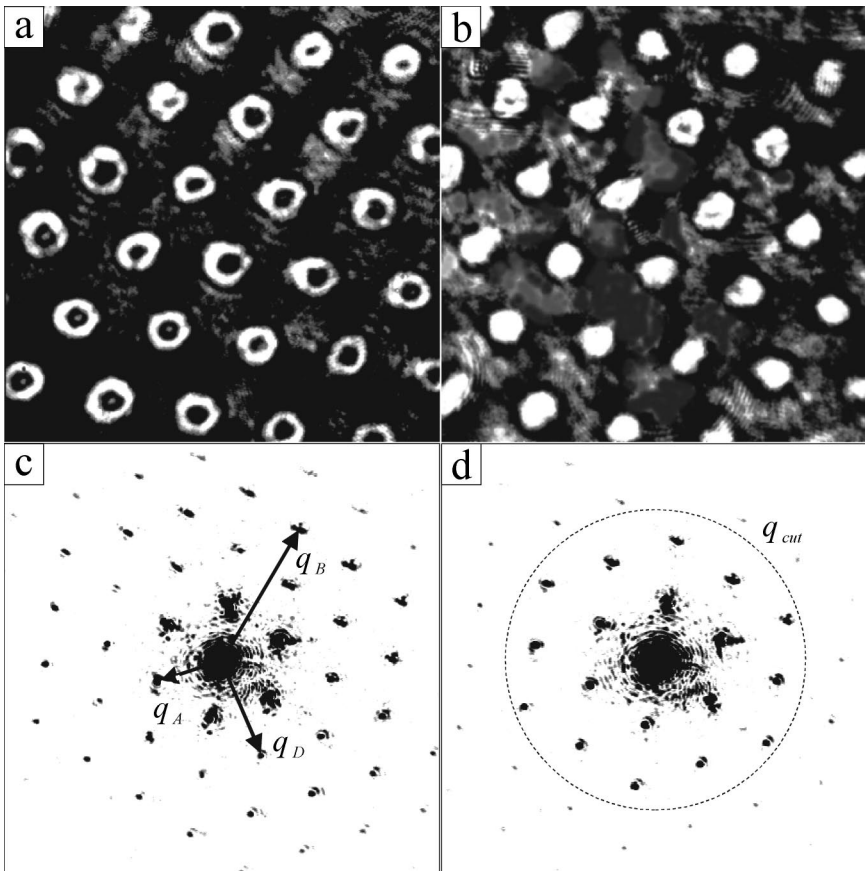

FIG. 4. Stimulated patterns (a) and (b) with corresponding spatial spectra (c) and (d) in a system without [(a) and (c)] and with [(b) and (d)] an additional low-pass amplitude filter [dashed circle in (d)] placed in front of the phase modulator. Arrows correspond to wave vectors $\mathbf{q}_A$, $\mathbf{q}_B$, and $\mathbf{q}_D$ used for the pattern formation analysis.
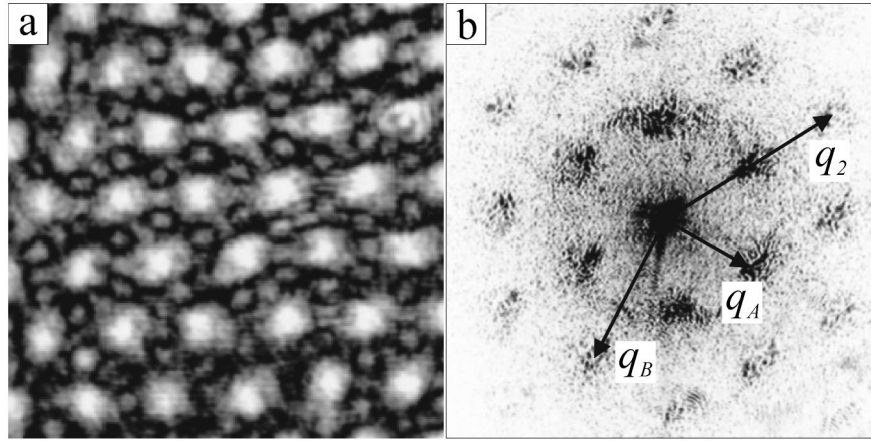
FIG. 5. Intensity distribution (a) and far-field spectrum (b) for the spatial filter shown in Fig. 1(b) ($\nu^{(0)}=1.1\pi$, $\nu^{(1)}=0.1\pi$, and $\nu^{(2)}=1.6\pi$).

C. Phase filter composed by concentric rings

Using the phase filter shown in Fig. 1(b), we observed the formation of spontaneous patterns resulting from interactions between spatial modes with wave vectors $\boldsymbol{q}_l$ having the two primary values of $|\boldsymbol{q}_l|=q_A$ and $|\boldsymbol{q}_l|=q_B$ [14]. The spontaneous pattern shown in Fig. 5(a) is composed of two coupled hexagons whose wave vectors yield the resonance condition $q_B \approx \sqrt{3} q_A$. Spectral components corresponding to the second spatial harmonic with wave number $q_2 = 2q_A$ are clearly seen in this pattern's spatial spectrum, shown in Fig. 5(b).

D. Off-axis spectral component phase control

A phase shift in the off-axis spectral component in the feedback was acheived in two ways. The first technique was to apply a voltage ν to a noncentral LC phase modulator element. A second method involved shifting the Zernike-type phase filter in a transverse direction with respect to the laser beam longitudinal axis. In the latter case, we were able to control the phase of off-axis spectral components having a wave number value less than the size of an individual LC element.

In experiments with off-axis spectral component phase control we observed waves traveling across the beam aperture, as shown in Fig. 6. The wave propagation direction $\boldsymbol{n}$ was parallel to the vector $\boldsymbol{q}_0$ corresponding to the center of the controlled off-axis LC element in the Fourier plane [Fig. 1(c)]. The traveling wave amplitude had an abrupt front, similar to shock waves studied in hydrodynamics (see, for example, [33]). The front of this wave typically was bent. When $|\boldsymbol{q}_0|$ was increased, the distortion of the front decreased while the wave's spatial frequency increased. Within the interval $0 < \nu < \pi$, traveling shock waves were not observed. The speed and amplitude of these shock waves were a function of the phase shift. The maximum value of the speed corresponded to a phase shift of $\nu \approx -\pi/2$.

III. MATHEMATICAL MODEL AND LINEAR STABILITY ANALYSIS

Consider the mathematical model for a LCLV diffractive feedback system with spatial filtering [34]. The field com-

plex amplitude in the Fourier filter output plane $A_{\mathrm{FF}}(\boldsymbol{r},t)$ is linked to the complex amplitude $A_{\mathrm{in}}\exp[iu(\boldsymbol{r},t)]$ of the wave reflected from the LCLV's internal mirror by the convolution integral
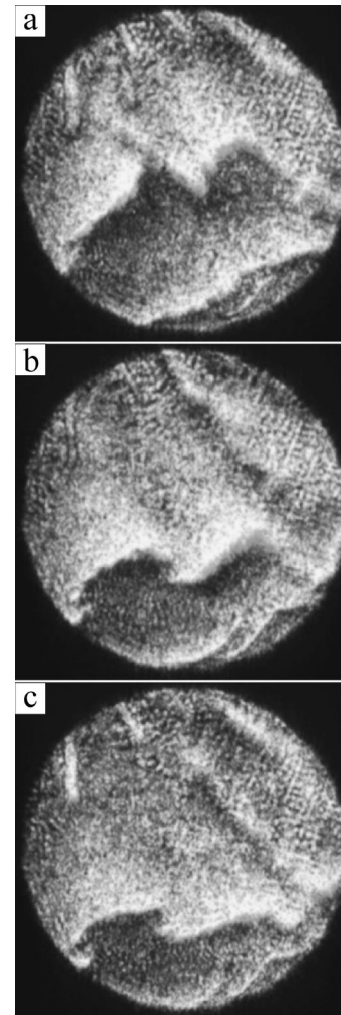

FIG. 6. Snaphots of near-field intensity distribution taken at three consequent moments separated in time by 30 ms for $\nu = -\pi/2$. The phase modulator was shifted by 0.5 mm in the transverse direction ($L = 20$ cm), and the aperture size was 15 mm.
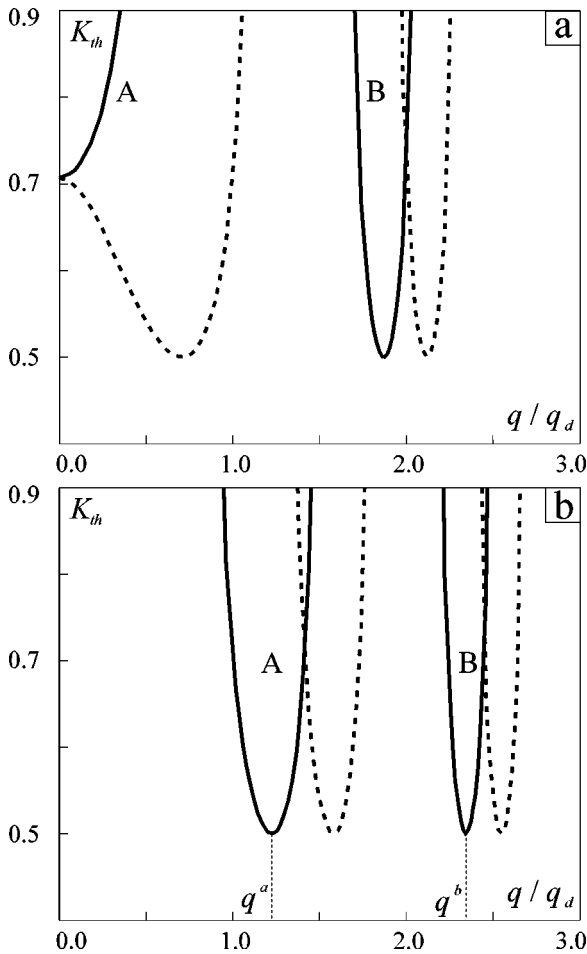
FIG. 7. Neutral stability curves for various phase shifts $\nu^{(0)}$: (a) $\nu^{(0)} = 0.25\pi$ (dashed line) and $\nu^{(0)} = 0.75\pi$ (solid line); (b) $\nu^{(0)} = 1.25\pi$ (dashed line) and $\nu^{(0)} = 1.75\pi$ (solid line).

$$A_{FF}(\mathbf{r},t) = \int A_{in} \exp[iu(\mathbf{r}',t)] h(\mathbf{r}'-\mathbf{r}) d^2\mathbf{r}', \qquad (1)$$

where $u(\mathbf{r},t)$ is a phase modulation introduced into the input plane wave A_{in} by the LCLV, and $h(\mathbf{r})$ is the Fourier transform of the spatial filter transfer function $T(\mathbf{q}) = \exp[iQ(\mathbf{q})]$. Diffraction over the distance L obeys the free-space propagation equation for the complex amplitude $A(\mathbf{r},z,t)$:

$$-2ik\frac{\partial A}{\partial z} = \Delta_\perp A, \qquad (2)$$

with boundary conditions $A(\mathbf{r},0,t) = A_{FF}(\mathbf{r},t)$ in the plane z_0. The phase modulation $u(\mathbf{r},t)$ depends on the feedback field's intensity distribution at the LCLV's photoconductive layer (plane z_1). In a simplified model describing LCLV dynamics, the phase $u(\mathbf{r},t)$ can be described by a nonlinear diffusion equation with Kerr-type nonlinearity [25,4]:

$$\tau\frac{\partial u}{\partial t} + u = d\Delta_\perp u + K I_{FB}(\mathbf{r},t), \qquad (3)$$

where τ and d are the LCLV time response and diffusion coefficients, K is the control parameter, $I_{FB}(\mathbf{r},t) = M(\mathbf{r})|A_{FB}(\mathbf{r},t)|^2$ is the feedback field intensity at the photoconductor layer, and $A_{FB}(\mathbf{r},t) = A(\mathbf{r},L,t)$. A more detailed
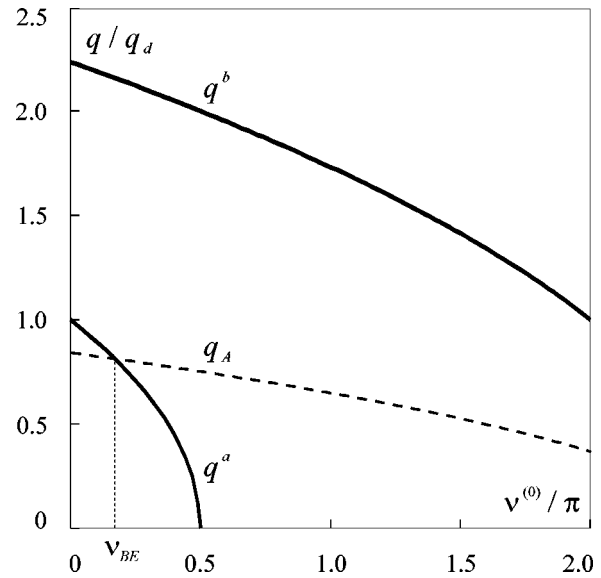

FIG. 8. Dependence of the instability ring radii q^a and q^b on the phase shift ν^0 (solid lines). The dashed line corresponds to the synchronization condition $q_A = 2q^b \sin(\phi/2)$ for the black-eye patterns (defined below).

mathematical model of LCLV dynamics that accounts for threshold and saturation properties can be found in [4,35].

First consider dynamics for the system of Eqs. (1)–(3) in the absence of the inserted mask $[M(\mathbf{r})=1]$. From linear stability analysis one can obtain the expression for a neutral stability surface [34]:

$$K_{th} = \frac{1+d|\mathbf{q}|^2}{2\sin[L|\mathbf{q}|^2/2k + Q(0) - Q(\mathbf{q})]}, \qquad (4)$$

where $\mathbf{q}$ is the perturbation transverse wave vector.

The spatially uniform solution to the system of Eqs. (1)–(3) becomes unstable when the control parameter $|K|$ exceeds a threshold value $K^{(0)}$. The threshold value $K^{(0)}$ and the corresponding wave vectors $\mathbf{q}^{(0)}$ for the most unstable modes are determined from the condition $K^{(0)} = \min|K_{th}(\mathbf{q})|$. For a rotationaly invariant spatial filter $Q(\mathbf{q}) = Q(q)$, we can write $K_{th}(\mathbf{q}) = K_{th}(q)$. In the case of weak diffusion the neutral stability curve $K_{th}(q)$ has several local minima with approximately the same threshold values $K^a \approx K^b \approx K^{(0)}$. In this case the unstable mode wave vectors are located at several instability rings with radii q^a, q^b, and so forth.

For a Zernike-type spatial filter $[Q(\mathbf{q}) = \nu^{(0)}$ for $\mathbf{q}=0$ and $Q(\mathbf{q})=0$ otherwise$]$ the neutral stability curves (instability balloons) are given by

$$K_{th} = \frac{1+dq^2}{2\sin\left(\frac{\pi}{2}(q/q_d)^2 + \nu^{(0)}\right)} \qquad (q \neq 0), \qquad (5)$$

where $q_d = \pi\sqrt{2/\lambda L}$. The first two instability balloons (A and B) are shown in Fig. 7. The locations of the instability balloon minima in $\mathbf{q}$ space can be controlled by changing the zero spectral component phase $\nu^{(0)}$, as shown in Fig. 8 for the first two instability balloons (A and B). Nonlinear interactions between unstable modes with wave numbers in the
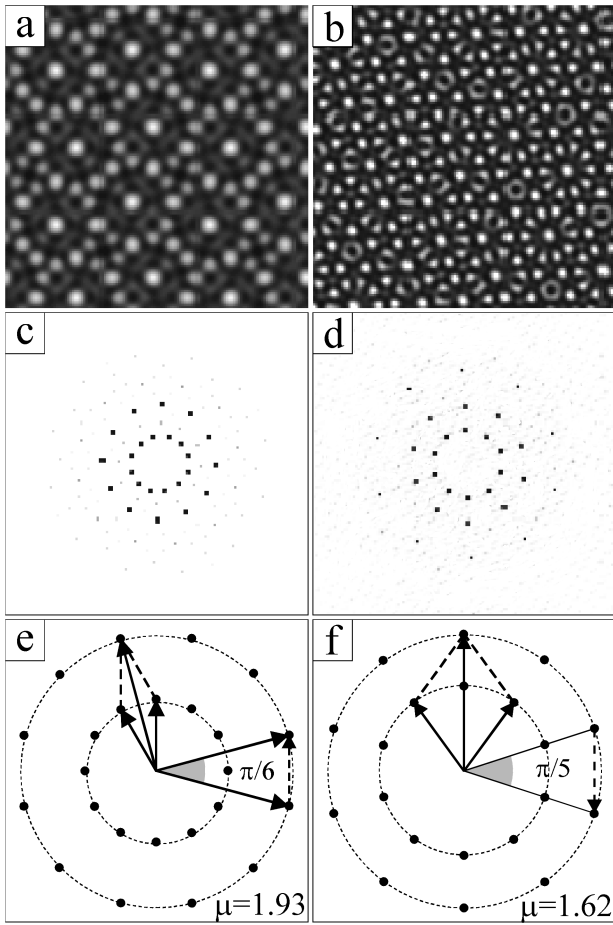
FIG. 9. Numerically obtained stationary state patterns (a) and (b) with corresponding spatial spectra (c) and (d) for $K = -0.55$ and $L = -0.02$: (a) dodecagon pattern ($\nu^{(0)} = -0.15\pi$), (b) decagon pattern ($\nu^{(0)} = 1.25\pi$). Schematic diagrams illustrate the elementary interactions between spectral components having different wave vectors for (e) dodecagon and (f) decagon patterns. Instability rings are shown by circles. The propagation length L is normalized by $ka^2/(2\pi)$, where a is the transverse pattern area size.

vicinity of different instability rings (i.e., belonging to different instability balloons) give rise to the formation of the patterns observed in our experiments.

IV. NUMERICAL SIMULATIONS

A. Zernike-type filter: Black-eye patterns

Numerical analysis of the original system of Eqs. (1)–(3) was performed with 128×128 and 256×256 uniform square grids. The diffusion coefficient was set to zero in order to have an identical minimum threshold value for different instability balloons ($K^a = K^b = K^{(0)}$) and thus provide effective interaction between active modes having different wave numbers. In our calculations we assumed the presence of a low-pass amplitude filter in the Fourier plane of the optical system feedback loop. This filter blocks all field spectral components with wave number $q > q_{\text{cut}}$ having the cutoff frequency $q_{\text{cut}} = 3q_d$. A fast Fourier transform routine was used to calculate the convolution integral (1) and to solve the free-space propagation equation (2). The value of the control parameter $|K|$ was near the onset of an instability threshold:
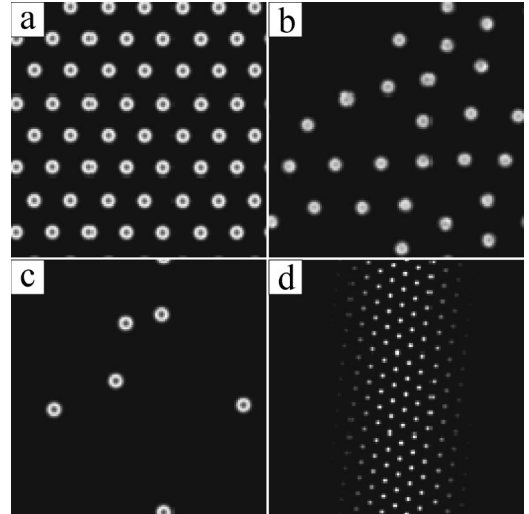

FIG. 10. Numerically obtained stationary state patterns for $K = -0.55$, $L = -0.01$, and various phase shift amplitudes $\nu^{(0)}$: (a) regular array of black eyes ($\nu^{(0)} = 0.25\pi$), (b) irregular black eyes ($\nu^{(0)} = 0.5\pi$), (c) localized states ($\nu^{(0)} = 0.8\pi$), (d) hexagonal array with low-frequency modulated amplitude ($\nu^{(0)} = 1.0\pi$).

$|K| = 1.1K^{(0)}$, where $K^{(0)} = 0.5$. As an initial condition $u(\mathbf{r}, t=0)$ we used realizations of a δ-correlated random field with small amplitude $|u(\mathbf{r}, t=0)| < 0.1$.

By varying the phase shift $\nu^{(0)}$ we observed transitions between patterns having different symmetries. In addition to hexagons, we obtained steady-state patterns that occurred due to the nonlinear coupling of modes with different wave numbers. The dodecagon-type patterns shown in Fig. 9(a) appeared in the phase shift amplitude range $-0.2\pi < \nu^{(0)} < 0.3\pi$. This type of pattern was observed previously in numerical simulations of the Kerr slice and feedback mirror system and in the nonlinear interferometer with diffractive feedback [36,14]. A new pattern with tenfold symmetry ("decagon"), shown in Fig. 9(b), was observed in the range $1.2\pi < \nu^{(0)} < 1.45\pi$. The spatial spectra for the dodecagon and decagon patterns along with the corresponding mode configurations illustrating nonlinear mode coupling are shown in Figs. 9(c)–9(f). The mode coupling parameter $\mu = q^b/q^a$ characterizing interaction between spatial modes belonging to different instability rings is $\mu = \sqrt{5} \approx 1.93$ for the
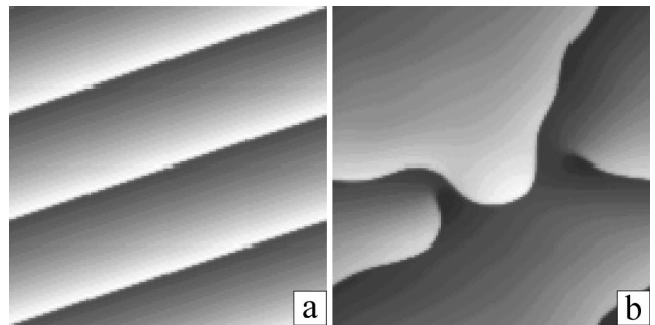

FIG. 11. Traveling wave patterns with $K = 20$ and $\nu = 1.5\pi$: (a) phase control of the single spectral component $\mathbf{q} = \mathbf{q}_0$, (b) phase control of spectral components in the circular spectral domain centered at $\mathbf{q} = \mathbf{q}_0$. The radius of the domain is equal to the LC element size.
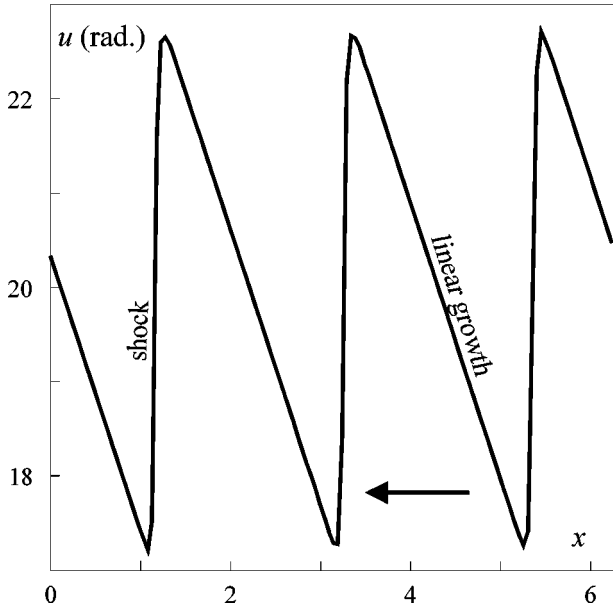
FIG. 12. Profile of traveling wave in Fig. 11(a) (x is dimensionless). The direction of wave propagation is indicated by the arrow.

dodecagon, and $\mu = 2\cos\pi/5 \approx 1.62$ for the decagon pattern.

Black-eye patterns were observed in numerical simulations within the interval $0.05\pi < \nu^{(0)} < 1.0\pi$ ($L<0$). As shown in Fig. 10, when $\nu^{(0)}$ was increased beyond $\pi/2$ the black-eye hexagon lattice [Fig. 10(a)] first transformed into an irregular array [Fig. 10(b)], and then into localized states [Fig. 10(c)]. At $\nu^{(0)} = \pi$, the black-eye patterns were replaced by low-frequency modulated hexagons [Fig. 10(d)]. Depending on initial conditions, different patterns can coexist for the same phase shift value $\nu^{(0)}$. For example, both dodecagons and black-eye arrays were found for $0.05\pi \leqslant \nu^{(0)} \leqslant 0.3\pi$.

B. Traveling waves

In the numerical simulations of the system having a spatial filter controlling the phase of a single off-axis element, we used the following phase transfer function model: $Q(\boldsymbol{q}) = \nu$ for $\boldsymbol{q} = \boldsymbol{q}_0$ and $Q(\boldsymbol{q}) = 0$ otherwise. We neglected diffraction so that $A_{FB}(\boldsymbol{r},t) = A_{FF}(\boldsymbol{r},t)$. Numerical simulations of Eqs. (1)–(3) were performed for various values of the parameters K and d. Above the threshold value $K > K^{(0)}$ we observed the formation of traveling waves. Examples of traveling wave patterns are given in Fig. 11. Slightly above the threshold, the traveling waves had a harmonic shape. When K increased, the shape of the wave became nonsymmetric. Far above the threshold value, the wave profile consisted of two regions, as seen in Fig. 12: a slow linear increase of the amplitude u in the direction of propagation, and a brief interval of abrupt fall. Waves with such a profile are known as shock waves [33]. When there was zero diffusion the shock wave did not move. The shock wave speed depended on the phase shift amplitude ν, with the maximum speed occurring at $\nu \approx 1.5\pi$. When q_0 was increased, the shock wave spatial frequency linearly increased. Calculations were also performed for an off-axis phase controlling element having a finite size. The result was wavefront bending similar to that observed in our experiments; compare the shock waves in Fig. 6 and in Fig. 11(b).
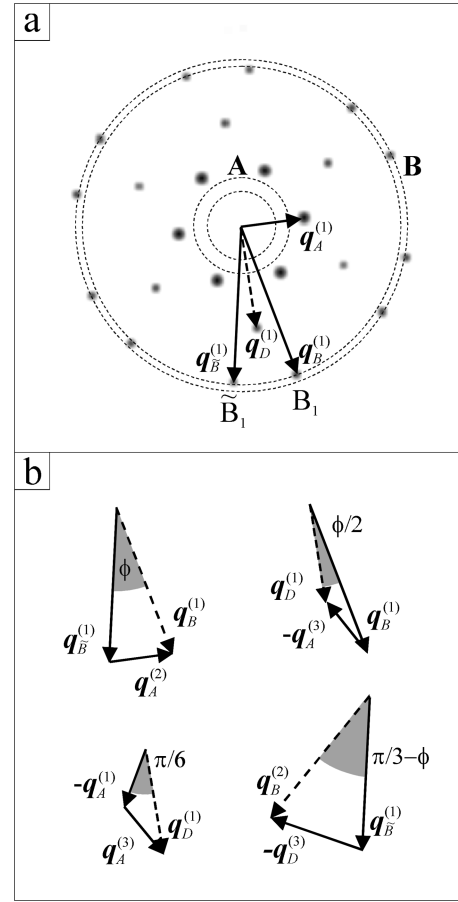

FIG. 13. Schematic diagram illustrating black-eye pattern formation: (a) spatial spectrum of the black-eye pattern in Fig. 10(a) (gray-level spots) together with wave vectors $\boldsymbol{q}_A^{(1)}$, $\boldsymbol{q}_B^{(1)}$, $\boldsymbol{q}_{\tilde{B}}^{(1)}$ belonging to different mode families, with instability rings (dotted circles) for $K = -0.55$; (b) wave-vector diagram showing elementary intermode interactions.

V. BLACK-EYE PATTERNS: NONLINEAR ANALYSIS

Consider the black-eye pattern in Fig. 10(a). This pattern's spatial spectrum is given in Fig. 13(a), together with the instability rings corresponding to the A and B instability balloons. Its spatial spectra consist of the 24 highest-intensity spectral components.

(i) Six spectral components $\boldsymbol{q}_A^{(j)}$ ($j=1,\ldots,6$) with equal wave numbers q_A forming a hexagon (A-hexagon mode family).

(ii) Six spectral components $\boldsymbol{q}_D^{(j)}$ ($j=1,\ldots,6$) having wave number q_D (D-hexagon mode family). The D-hexagon mode family is rotated by $\pi/6$ with respect to the A hexagon.

(iii) Twelve spectral components $\boldsymbol{q}_B^{(j)}$ and $\boldsymbol{q}_{\tilde{B}}^{(j)}$ with wave number $q_B \approx q^b$ belonging to two hexagon manifolds (B- and $\tilde{B}$-hexagon mode families). B and $\tilde{B}$ hexagons are mutually rotated by an angle ϕ.

From the black-eye pattern spatial spectrum in Fig. 13(a), we can see that only spectral components $\boldsymbol{q}_B^{(j)}$ and $\boldsymbol{q}_{\tilde{B}}^{(j)}$ belong to the instability ring and hence have positive eigenvalues $\lambda_{B,\tilde{B}}^{(j)} \geqslant 0$ (active modes). Here $\lambda_{B,\tilde{B}}^{(j)} = -(1+dq_{B,\tilde{B}}^2) + 2K\sin[\pi/2(q_{B,\tilde{B}}/q_d)^2 + \nu^{(0)}]$. The most distinguishing feature of the spectrum in Fig. 13(a) is that modes correspond-

ing to A- and D-hexagon mode families do not belong to the instability rings, and hence have negative eigenvalues $\lambda_A^{(j)} < 0$ and $\lambda_D^{(j)} < 0$ (passive modes). These modes would die if they were not driven by modes belonging to B and $\widetilde{B}$ manifolds.

Qualitative analysis of the black-eye mode configuration suggests that black-eye pattern formation occurs due to intermode interaction, resulting in the coupling of all four hexagon mode manifolds. A schematic diagram of interactions between modes belonging to different mode families is shown in Fig. 13(b). From a consideration of the wave-vector geometry in Fig. 13 we obtain the following mode synchronization conditions:

$$q_A = 2q_B \sin(\phi/2),$$

$$q_D = \sqrt{3} q_A, \tag{6}$$

$$q_A^2 = q_D^2 + q_B^2 - 2q_D q_B \cos(\phi/2).$$

From this expression we find the angle between B and $\widetilde{B}$ hexagons to be $\phi = \phi_{BE} = \arccos(13/14) \approx 21.8°$, and the mode coupling parameter to be $\mu = \mu_{BE} = q_B/q_A = \sqrt{7}$. The dependence $q_A(\nu^{(0)}) = 2q^b(\nu^{(0)})\sin\phi/2$ is shown in Fig. 8 as a function of the controlling phase shift $\nu^{(0)}$. At the point corresponding to $\nu^{(0)} = \nu_{BE} = \pi/6$, we have the resonant condition for black-eye pattern formation: $q_A = q^a$. For this case, modes belonging to the A-hexagon manifold are active ($\lambda_A^{(j)} \geq 0$) and the corresponding wave vectors $q_A^{(j)}$ are located inside the instability ring. When the parameter $\epsilon = |\nu^{(0)} - \nu_{BE}|$ is increased, the mismatch between wave numbers q_A and q^a also increases, thus expanding the mismatch between the A-hexagon manifold and the instability ring, as seen in Fig. 13(a). Increasing ϵ changes the eigenvalue sign ($\lambda_A^{(j)} < 0$), and subsequently as the absolute values $|\lambda_A^{(j)}|$ grow the black-eye patterns eventually disintegrate when $\epsilon > 0.3\pi$.

One question that naturally arises is why are the developed black-eye pattern modes belonging to B- and $\widetilde{B}$-hexagon mode families always matched with the instability ring, but the A-hexagon mode manifold is not? In other words, why does the system choose the resonance condition $q_B = q^b$ over the condition $q_A = q^a$? The physical reason for such a preference is related to the shape of the instability curves shown in Fig. 14. The B branch of the instability curve is narrower. As a result, any small mismatch between wave-number values q_B and q^b causes a rapid decrease in the eigenvalues $\lambda_{B,\widetilde{B}}^{(j)}$. On the contrary, the same amplitude mismatch between wave numbers q_A and q^a does not produce as great a decrease in the eigenvalues $\lambda_A^{(j)}$. A similar phenomenon that occurred with the dodecagon pattern was analyzed on the basis of mode amplitude equations in [14]. It was shown that due to the difference in instability balloon width the wave vectors were locked into the more narrow one.

The process of B- and $\widetilde{B}$-hexagon manifold locking is illustrated in Fig. 14, where spatial spectrum evolution for the function $u(\mathbf{r},t)$ is shown at the beginning of the pattern formation process, and for the stationary state black-eye pat-
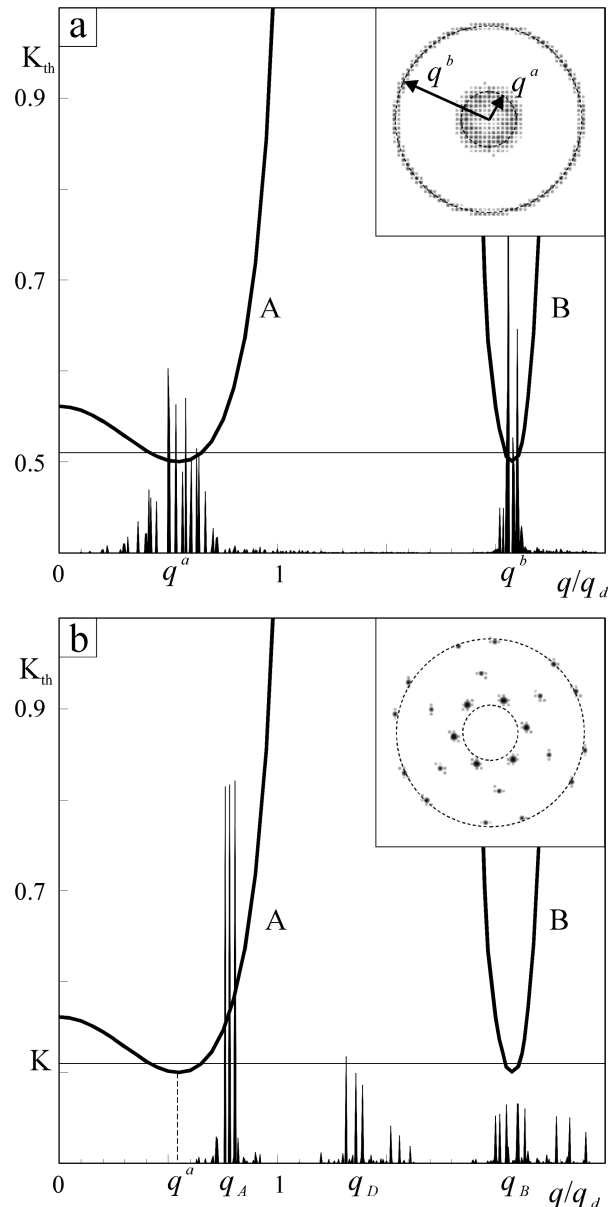

FIG. 14. Evolution of the black-eye pattern spatial spectrum for $K = -0.55$ (horizontal line) and $\nu^{(0)} = 0.3\pi$: (a) $t = 50\tau$ and (b) $t = 5000\tau$. Azimuthally averaged spatial spectra are given along with the neutral stability curves (solid lines); the 2D spectra at the top right are shown with the instability circles of radius q^a and q^b.

tern. At an earlier stage in the pattern formation process [Fig. 14(a)] wave vectors of the most unstable perturbation components are located at the bottom of the neutral stability curves (inside the instability rings). In this case $q_A \approx q^a$. With mode amplitude growth, interactions between modes having wave numbers belonging to different instability balloons lead to wave-number amplitude q_A change (A-hexagon mode manifold mismatch) and the appearance of additional spectral components with wave numbers $q \approx q_D$ corresponding to the D-hexagon mode family [Fig. 14(b)]. For the stationary state black-eye pattern in Fig. 14(b) the synchronization conditions (6) [$\mu = \mu_{BE}$ and $\phi = \phi_{BE}$] obtained from geometrical consideration are sufficiently accurate.

For the nonlinear analysis of black-eye patterns we use a Neumann-series approach [37,14]. This technique is applied here to derive the system of amplitude equations for the mode configuration shown in Fig. 13. Small perturbations of the system's stationary state spatially uniform solution involve four hexagon manifolds:

$$\widetilde{u}(\boldsymbol{r},t)=\sum_{j=1}^{6}\{a_j(t)\exp[i\boldsymbol{q}_A^{(j)}\cdot\boldsymbol{r}]+d_j(t)\exp[i\boldsymbol{q}_D^{(j)}\cdot\boldsymbol{r}]$$
$$+b_j(t)\exp[i\boldsymbol{q}_B^{(j)}\cdot\boldsymbol{r}]+\widetilde{b}_j(t)\exp[i\boldsymbol{q}_{\widetilde{B}}^{(j)}\cdot\boldsymbol{r}]\},\quad(7)$$

where $a_j(t)$, $d_j(t)$, $b_j(t)$, and $\widetilde{b}_j(t)$ are the mode amplitudes. The wave vectors $\boldsymbol{q}_A^{(j)}$, $\boldsymbol{q}_D^{(j)}$, $\boldsymbol{q}_B^{(j)}$, and $\boldsymbol{q}_{\widetilde{B}}^{(j)}$ satisfy the conditions (6) for $q_B=q^b$.

Substitute perturbation (7) into Eqs. (1)–(3) and keep only terms up to the second order in the Neumann-series expansion. For $\widetilde{u}(\boldsymbol{r},t)$ to be real, assume $a_4=a_1$, $a_5=a_2$, $a_6=a_3$, and the same condition for the amplitudes d_j, b_j, and $\widetilde{b}_j$. The resulting equations for the mode amplitudes forming the black-eye pattern are

$$\tau\dot{b}_j+b_j=4KD\{S_bQ(b_j)+2[C_bQ(b_{[j+1]})Q(b_{[j+2]})$$
$$+P_{ab}Q(\widetilde{b}_j)Q(a_j)+P_{adb}Q(a_{[j+1]})Q(d_j)$$
$$+P_{db}Q(d_{[j+1]})Q(\widetilde{b}_{[j+2]})]\},$$

$$\tau\dot{\widetilde{b}}_j+\widetilde{b}_j=4KD\{S_bQ(\widetilde{b}_j)+2[C_bQ(\widetilde{b}_{[j+1]})Q(\widetilde{b}_{[j+2]})$$
$$+P_{ab}Q(b_j)Q(a_j)+P_{adb}Q(a_{[j+2]})Q(d_j)$$
$$+P_{db}Q(d_{[j+2]})Q(b_{[j+1]})]\},$$

$$\tau\dot{a}_j+a_j=4KD(S_aQ(a_j)+2\{C_aQ(a_{[j+1]})Q(a_{[j+2]})$$
$$+P_{ba}Q(b_j)Q(\widetilde{b}_j)+P_{da}[Q(d_{[j+2]})Q(a_{[j+1]})$$
$$+Q(d_{[j+1]})Q(a_{[j+2]})]$$
$$+P_{bda}[Q(b_{[j+2]})Q(d_{[j+2]})$$
$$+Q(\widetilde{b}_{[j+1]})Q(d_{[j+1]})]\}),\quad(8)$$

$$\tau\dot{d}_j+d_j=4KD(S_dQ(d_j)+2\{C_dQ(d_{[j+1]})Q(d_{[j+2]})$$
$$+P_{ad}Q(a_{[j+1]})Q(a_{[j+2]})$$
$$+P_{abd}[Q(b_j)Q(a_{[j+1]})+Q(\widetilde{b}_j)Q(a_{[j+2]})]$$
$$+P_{bd}Q(b_{[j+2]})Q(\widetilde{b}_{[j+1]})\}).$$

In Eqs. (8), $Q(\cdot)\equiv J_1(\cdot)/J_0(\cdot)$, $D=\Pi_{j=1}^3 J_0(a_j)J_0(b_j)J_0(b_j)J_0(\widetilde{b}_j)$, and $[j]=(j\bmod3)$. The coefficients in Eqs. (8) are expressed as follows:

$$S_{a,b,d}=\sin\left(\frac{\pi}{2}(q_{A,B,D}/q_d)^2+\nu^{(0)}\right),$$

$$C_{a,b,d}=1-\cos\left(\frac{\pi}{2}(q_{A,B,D}/q_d)^2+\nu^{(0)}\right),$$

$$P_{ab}=\cos\left(\frac{\pi}{2}(q_A/q_d)^2-\frac{\pi}{2}(q_B/q_d)^2\right)$$
$$-\cos\left(\frac{\pi}{2}(q_B/q_d)^2+\nu^{(0)}\right),$$

$$P_{ad}=1-\cos\left(\frac{\pi}{2}(q_D/q_d)^2+\nu^{(0)}\right),$$

$$P_{da}=\cos\left(\frac{\pi}{2}(q_D/q_d)^2-\frac{\pi}{2}(q_A/q_d)^2\right)$$
$$-\cos\left(\frac{\pi}{2}(q_A/q_d)^2+\nu^{(0)}\right),$$

$$P_{db}=\cos\left(\frac{\pi}{2}(q_D/q_d)^2-\frac{\pi}{2}(q_B/q_d)^2\right)$$
$$-\cos\left(\frac{\pi}{2}(q_B/q_d)^2+\nu^{(0)}\right),$$

$$P_{bd}=1-\cos\left(\frac{\pi}{2}(q_D/q_d)^2+\nu^{(0)}\right),$$

$$P_{adb}=2\left[\cos\left(\frac{\pi}{2}(q_A/q_d)^2-\frac{\pi}{2}(q_D/q_d)^2\right)\right.$$
$$\left.-\cos\left(\frac{\pi}{2}(q_B/q_d)^2+\nu^{(0)}\right)\right],$$

$$P_{bda}=2\left[\cos\left(\frac{\pi}{2}(q_B/q_d)^2-\frac{\pi}{2}(q_D/q_d)^2\right)\right.$$
$$\left.-\cos\left(\frac{\pi}{2}(q_A/q_d)^2+\nu^{(0)}\right)\right],$$

$$P_{abd}=2\left[\cos\left(\frac{\pi}{2}(q_A/q_d)^2-\frac{\pi}{2}(q_B/q_d)^2\right)\right.$$
$$\left.-\cos\left(\frac{\pi}{2}(q_D/q_d)^2+\nu^{(0)}\right)\right].$$

A complete analysis of the system of amplitude Eqs. (8) and the stability properties of the solutions is beyond the framework of the present study and will be done elsewhere. Nevertheless, it can be shown that the solution of Eqs. (8) in the form $b_j=\widetilde{b}_j$, $|b_j|=b$, and $b_1b_2b_3<0$ (negative hexagons), and $|a_j|=a$ and $a_1a_2a_3>0$ (positive hexagons), $|d_j|=0$, corresponds to the hexagonal array of black eyes. In contrast with the dodecagon-type pattern consisting of four positive hexagonal manifolds [14], black-eye pattern formation occurs due to the nonlinear coupling of hexagonal manifolds having different signs.

VI. CONCLUSION

By controlling the feedback field spectral component phase in a nonlinear system with LCLV and diffractive feedback, we were able to realize controlled transitions between spatio-temporal regimes, and to obtain patterns not previ-

ously observed in optics. Analysis of black-eye patterns composed of modes with both positive and negative eigenvalues demonstrates the importance of interaction between active and passive modes in the pattern formation process. Further use of high-resolution spatial phase modulators will create wide opportunities for design and control of a variety of dynamical regimes.

[1] G. Giusfredy, J. F. Valley, R. Pon, G. Khitrova, and H. M. Gibbs, J. Opt. Soc. Am. B **5**, 1181 (1988).

[2] Chaos Solitons Fractals **4**, 1251 (1994), special issue on *Nonlinear Optical Structures, Patterns, Chaos*, edited by L. A. Lugiato and M. S. El Nashie.

[3] G. Grynberg, E. Le Bihan, P. Verkerk, P. Simoneau, J. R. R. Leite, D. Bloch, S. Le Boiteux, and M. Ducloy, Opt. Commun. **67**, 363 (1988).

[4] *Self-Organization in Optical Systems and Applications in Information Technology*, edited by M. A. Vorontsov and W. B. Miller (Springer, Berlin, 1995).

[5] M. Tamburrini, M. Bonavita, S. Wabnitz, and E. Santamato, Opt. Lett. **18**, 855 (1993).

[6] T. Honda, Opt. Lett. **18**, 598 (1993).

[7] J. Glückstad and M. Saffman, Opt. Lett. **20**, 551 (1995).

[8] D. Dangoisse, D. Hennequin, C. Lepers, E. Louvergneaux, and P. Glorieux, Phys. Rev. A **46**, 5955 (1992).

[9] T. Ackemann, Yu. A. Logvin, A. Heuer, and W. Lange, Phys. Rev. Lett. **75**, 3450 (1995).

[10] K. Staliunas and C. O. Weiss, Physica D **81**, 79 (1995).

[11] M. Le Berre, D. Leduc, E. Ressayre, and A. Tallet, Phys. Rev. A **54**, 3428 (1996).

[12] S. Residori, P. L. Ramazza, E. Pampaloni, S. Bocceleti, and F. T. Arecchi, Phys. Rev. Lett. **76**, 1063 (1996).

[13] A. A. Afanas'ev, Yu. A. Logvin, A. M. Samson, and B. A. Samson, Opt. Commun. **115**, 559 (1995).

[14] M. A. Vorontsov and A. Yu. Karpov, J. Opt. Soc. Am. B **14**, 34 (1997).

[15] W. J. Firth, J. Mod. Opt. **37**, 151 (1990).

[16] M. Brambilla, A. Gatti, L. A. Lugiato, and F. Prati, in *Chaos, Solitons and Fractals*, edited by L. Lugiato (Pergamon, New York, 1994), p. 1277.

[17] W. J. Firth and A. J. Scroggie, Phys. Rev. Lett. **76**, 1623 (1996).

[18] M. Tlidi, P. Mandel, and R. Lefever, Phys. Rev. Lett. **73**, 640 (1994).

[19] B. A. Samson and M. V. Vorontsov, Phys. Rev. A **56**, 1621 (1997).

[20] P. K. Jakobsen, J. Lega, Q. Feng, M. Staley, J. V. Moloney, and A. C. Newell, Phys. Rev. A **49**, 4189 (1994); J. Lega, P. K. Jakobsen, J. V. Moloney, and A. C. Newell, *ibid.* **49**, 4201 (1994).

[21] R. Lopez-Ruiz, G. B. Mindlin, C. Pérez-Garcia, and J. R. Tredicce, Phys. Rev. A **49**, 4916 (1994).

[22] F. T. Arecchi, A. V. Larichev, P. L. Ramazza, S. Residori, J. C. Ricklin, and M. A. Vorontsov, Opt. Commun. **117**, 492 (1995).

[23] W. Lu, D. Yu, and R. G. Harrison, Phys. Rev. Lett. **76**, 3316 (1996).

[24] R. Martin, A. J. Scroggie, G.-L. Oppo, and W. J. Firth, Phys. Rev. Lett. **77**, 4007 (1996).

[25] S. A. Akhmanov, M. A. Vorontsov, V. Yu. Ivanov, A. V. Larichev, and N. I. Zheleznykh, J. Opt. Soc. Am. B **9**, 78 (1992).

[26] G. D'Alessandro and W. J. Firth, Phys. Rev. A **46**, 537 (1992).

[27] M. A. Vorontsov, Quantum Electron. **23**, 269 (1993).

[28] M. Tamburrini, E. Ciaramella, and E. Santamato, in *Chaos, Solitons and Fractals*, edited by L. Lugiato, (Pergamon, New York, 1994), p. 1355.

[29] J. W. Goodman, *Introduction to Fourier Optics* (McGraw-Hill, New York, 1996).

[30] M. A. Vorontsov and A. Yu. Karpov, J. Mod. Opt. **44**, 439 (1997).

[31] F. H. Busse, Rep. Prog. Phys. **41**, 28 (1978).

[32] G. H. Gunaratne, Q. Ouyang, and H. L. Swinney, Phys. Rev. E **50**, 2802 (1994).

[33] G. B. Whitham, *Linear and Nonlinear Waves* (John Wiley and Sons, New York, 1974).

[34] E. V. Degtiarev and M. A. Vorontsov, J. Opt. Soc. Am. B **12**, 1238 (1995).

[35] R. Neubecker, G.-L. Oppo, B. Thuering, and T. Tschudi, Phys. Rev. A **52**, 791 (1995).

[36] E. V. Degtiarev and M. A. Vorontsov, J. Mod. Opt. **43**, 93 (1996).

[37] M. A. Vorontsov and W. J. Firth, Phys. Rev. A **49**, 2891 (1994).